Soft Matter

PAPER

View Article Online
View Journal | View Issue

Cite this: *Soft Matter*, 2023, **19**, 999

Three-dimensional liquid crystal polymer actuators assembled by athermal photo-welding†

Yaoqing Feng,[a] Jia Wei,[a] Lang Qin *[a] and Yanlei Yu *[ab]

Received 9th November 2022,
Accepted 29th December 2022

DOI: 10.1039/d2sm01476a

rsc.li/soft-matter-journal

Photodeformable liquid crystal polymers (LCPs) exhibit shape changes of different modes like bending, twisting, and oscillation, which depend on the orientation of liquid crystals. However, it is challenging to create a three-dimensional (3D) actuator with distinct actuation modes due to the difficulty of local orientation in a complex bulk architecture. Here we propose a strategy based on athermal photo-welding to integrate different orientations into a single flexible actuator by the photofluidization of azobenzene-containing linear LCPs. Stretch-induced uniaxial films are cut in different directions and subsequently welded *via* local photofluidization, during which the LCP transitions from a high-modulus glassy state to a rubbery state upon photoisomerization of azobenzene at room temperature. As a consequence, a cucumber vine-like structure with the opposite handedness and a lifting gripper are constructed by such a cut-and-weld process, demonstrating diverse deformation modes of winding, unwinding, and curling. This strategy provides an athermal process for the fabrication of seamless 3D flexible actuators without structural defects, which have potential applications in micromechanical systems, soft robotics, and artificial muscles.

Introduction

Smart materials have received extensive attention in the fields of soft robots, biomimetic devices, sensors, intelligent control systems, and artificial intelligence.[1–6] Photodeformable liquid crystal polymers (LCPs) combine the external field responsiveness of liquid crystals (LCs), intermolecular synergy, and the excellent mechanical properties of polymers, which are one of the ideal smart materials for constructing flexible actuators.[7–12] Recently, researchers have been particularly interested in 3D LCP actuators with different deformation modes, which exhibit a high degree of collective or individual motion for the execution of advanced tasks.[13–17] The LC orientations, such as planar, homeotropic, twisted, and splayed, are significant, and determine the deformation modes of actuators.[18–20] However, the methods of constructing complex 3D LCP actuators with distinct local orientations are limited to the complex photo-orientation technique, which requires multiple programmed steps to operate and it is difficult to obtain diverse orientations using the technique.[21–24]

Recently, welding processes have been considered to be a viable solution to build flexible 3D actuators with diverse LC orientations through chemical bonding,[25–27] including secondary polymerization,[28,29] as well as network reconstruction based on dynamic bonds.[30–34] Secondary polymerization for further cross-linking can be triggered by light or heat to realize defect-free welding of two LCP films with redundant reactive groups or crosslinkers. Ji and Wei *et al.* created seamless multi-component 3D LCP robots by means of thermal secondary polymerization of reactive acrylate groups in preformed acrylate group-rich LCP films, simultaneously realizing the welding of LCP films and uniaxial orientation of mesogens.[29] However, the polymer network will be completely fixed once the reactive group is depleted, and excessive cross-linking reactions may damage the mechanical properties of LCPs.[26] Recently, dynamic covalent bonds such as dynamic ester, dynamic boroxines, and diselenide bonds have been applied to prepare assembled LCP actuators, depending on the rearrangement of dynamic networks between two films. Yang *et al.* synthesized monodomain LCP films with exchangeable disulfide bonds through *in situ* photopolymerizations in antiparallel surface-rubbed cells, cut the obtained uniaxial-aligned LCP films into pieces and pasted them together *via* dynamic disulfide exchange to form versatile shaped soft actuators.[31] However, the breaking and reforming procedure of dynamic covalent bonds usually requires a high temperature or the assistance of other reagents, which may disrupt the originally designed LC orientations, or lead to the poor performance of actuators with the residues of auxiliary reagents.[33] Therefore, an alternative

[a] *Department of Materials Science, State Key Laboratory of Molecular Engineering of Polymers, Fudan University, 220 Handan Road, Shanghai, 200433, China. E-mail: ylyu@fudan.edu.cn, qinlang@fudan.edu.cn*
[b] *Yiwu Research Institute of Fudan University, Chengbei Road, Yiwu City, Zhejiang 322000, P. R. China*

† Electronic supplementary information (ESI) available: Synthetic routes of the monomers and liquid crystal polymers, liquid crystal orientation characterization, and photodeformation behaviour investigations of the liquid crystal polymer films. See DOI: https://doi.org/10.1039/d2sm01476a

technique for athermal welding is urgently needed to assemble LCPs with different orientations into a 3D actuator.

Photofluidization is an athermal photo-welding method based on photoisomerization reactions, which are induced by photoresponsive groups such as azobenzene.[35–37] Azobenzene-containing polymers (azopolymers) exhibit photoinduced reversible solid-to-liquid transitions due to the photoswitchable glass transition temperature (T_g), which have been utilized for the welding of polymers.[38,39] Under UV irradiation, the T_g of the azopolymer decreases lower than room temperature, while the polymer transitions from a glassy state to a rubbery state or even a viscous state without heating. By welding the fluidized polymers *via* surface fusion and the entanglement of molecular chains, LCPs with diverse LC orientations are integrated to create 3D actuators.

Here, the azobenzene-containing linear LCPs are assembled into 3D complex actuators with different LC orientations by photofluidization (Fig. 1a), which has been comprehensively investigated in the perspective of chemical structures. Ring-opening metathesis polymerization (ROMP) is employed to synthesize a series of LCPs with different side chain mesogens. Photo-welded bilayer films are fabricated *via* a photofluidization process, in which molecular chains of two fluidized films entangle and the surface fuses together with pressure. Taking advantage of this cut-and-weld process, a cucumber vine-like structure with opposite handedness is produced using a photo-welded LCP ribbon with different orientations upon UV irradiation (Fig. 1b). In addition, a light-controlled lifting gripper is fabricated with LCP ribbons of different orientations, and it reveals individual motion to execute diverse functions. We anticipate that photo-welding can become a facile process to obtain complex bulk architectures of LCPs, thus providing far-reaching possibilities for soft microdevices with advanced functionalities.

Experimental

Materials

Azobenzene, cyclooctene, biphenyl, and phenyl benzoate monomers were obtained according to the published articles.[6,40,41] The chemicals used in synthesis were all commercially available without further purification.

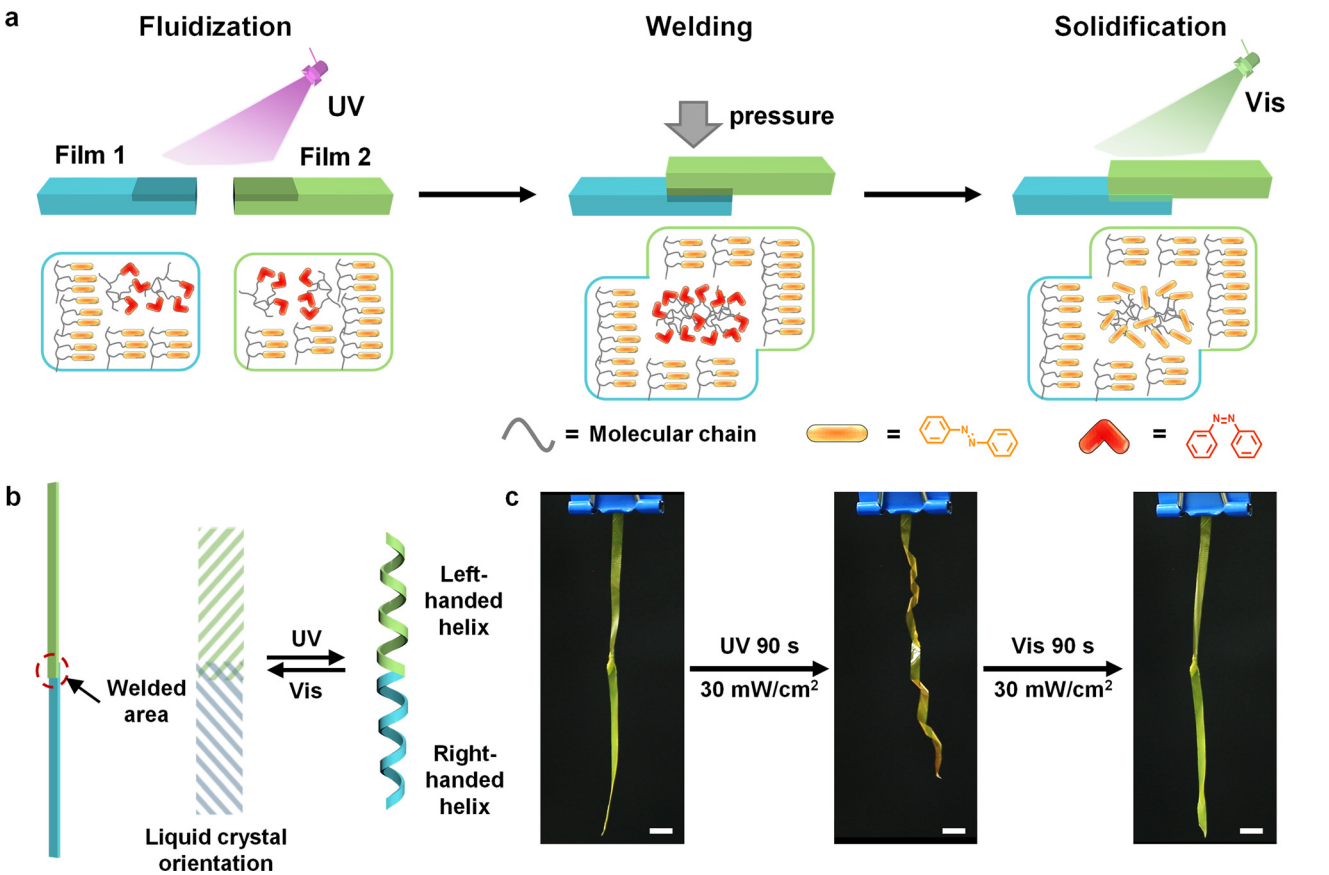

Fig. 1 (a) Schematic presentation of the photo-welding process. Only the area exposed to UV irradiation undergoes fluidization based on photoisomerization of azobenzene groups. Two films are welded together at the fluidized area with pressure, resulting from the entanglement of molecular chains. By the irradiation of visible light, the fused area is cured and the films are seamlessly welded. (b) Schematic illustration showing the photodeformation behavior of a photo-welded LCP ribbon. Lines in the picture refer to the LC orientations. (c) Photographs showing that a photo-welded ribbon with different LC orientations displays a cucumber vine-like structure with opposite handedness upon UV irradiation (λ = 365 nm), and then unwinds to its initial state upon irradiation with visible light (λ = 530 nm). The scale bar is 5 mm.

Synthesis of LCPs

The chemical structures of P1, P2, and P3 are outlined in Fig. 2a, and the synthetic routes are described in the ESI† (Fig. S1–S3).

The polymerization of P1 was performed using standard Schlenk techniques under a nitrogen atmosphere. The azobenzene monomer (1.354 g, 2 mmol) and cyclooctene monomer (0.132 g, 1.2 mmol) were added into a Schlenk flask. Then, the 3 μmol second-generation Grubbs catalyst with 3 mL anhydrous dichloromethane was added to the mixture. After stirring for 1 h at 50 °C, a yellow solid polymer was precipitated from methanol. (1.332 g, 91%). P2 and P3 were synthesized according to the published works,[40,41] and the yields were 94% and 90%, respectively. All the results of ^{1}H NMR are shown in the ESI† (Fig. S1–S3).

Characterization of LCPs

^{1}H NMR spectra of the monomers and the linear LCPs were recorded on a Bruker AVANCE III HD NMR spectrometer using tetramethyl silane as the internal standard and $CDCl_3$ as the solvent. The molecular weights of the polymers and their polydispersity indices were measured by gel permeation chromatography (GPC, Waters, E2695) using tetrahydrofuran as the eluent at a flow rate of 1 mL min^{-1}. *Cis* LCPs were prepared according to the published work.[38] The *trans* LCPs were dissolved in CH_2Cl_2, followed by irradiating with UV light (365 nm, 100 mW cm^{-2}) under stirring in the solution to prepare enough *cis* LCPs for the DSC measurement. Then CH_2Cl_2 was removed under vacuum (7 mbar, 30 min). The thermodynamic properties of the obtained *trans* and *cis* LCPs were determined by differential scanning calorimetry (DSC, TA, Q2000) at a heating and cooling rate of 10 °C min^{-1}. The temperature interval was −60–150 °C. The photoisomerization of LCPs was characterized by ultraviolet and visible spectrophotometry (UV-Vis, PerkinElmer, Lambda 650).

Photofluidization and photo-welding of LCP films

The LCP films were prepared by the drop-casting method and annealed for 12 h at the temperature that was 15 °C below the clearing point. The thickness of the LCP films is 20 μm. 365 nm UV light was generated using an Omron ZUV-H30MC light source with a ZUV-C30H controller. 530 nm visible light was generated using a CCS HLV-24GR-3W. The LCP films were exposed to UV light (365 nm, 100 mW cm^{-2}) for 2 min to prepare a *cis*-rich surface for the characterization of the surface

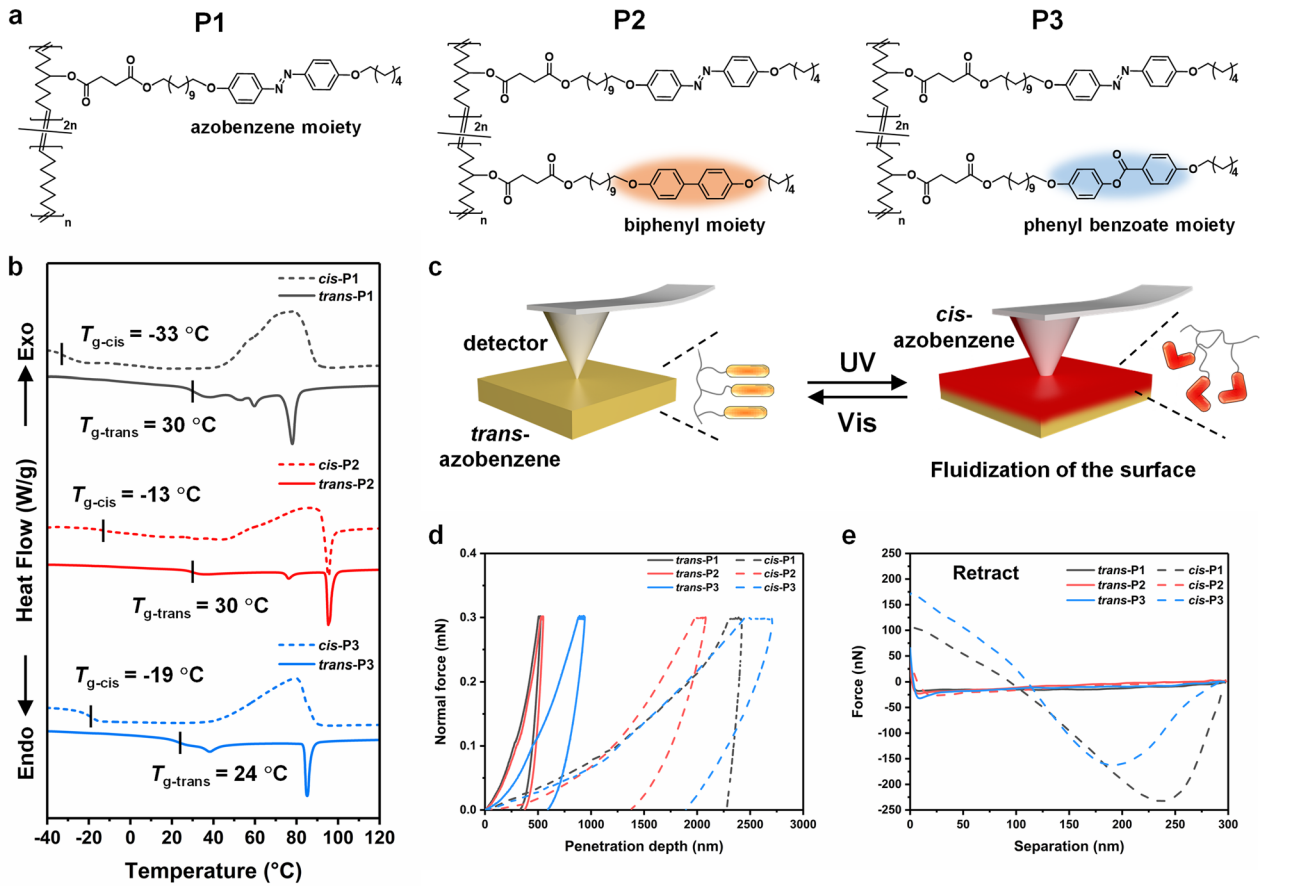

Fig. 2 Photofluidization of LCP films. (a) Chemical structures of LCPs. (b) DSC heating curves of *trans* LCPs (solid line) and *cis* LCPs (dashed line). The wide exothermic peaks in the heating curves of *cis* LCPs show the *cis*-to-*trans* transformation of azobenzene groups. (c) Schematic illustration showing surface mechanical properties of LCP films before and after UV irradiation with nanoindentation and fast-scan AFM. (d) Loading-pause-unloading displacement curves of the P1, P2, and P3 films before and after UV irradiation (365 nm, 100 mW cm^{-2}, 2 min). The penetration depth of *cis* films significantly increases. (e) Force–separation curves of the P1, P2, and P3 films before and after UV irradiation (365 nm, 100 mW cm^{-2}, 2 min).

properties. The surface hardness of LCP films was measured using an ultra-nanoindentation tester (CSM, UNHT) with a diamond intender. The indentation was carried out totally 9 times with the same test parameters, and the data obtained were averaged. Approach/retract speed: 2000 nm min^{-1}, max load: 0.30 mN, loading/unloading rate: 0.30 mN min^{-1}, and pause: 30.0 s. The experimental temperature was 25 °C. The surface adhesion was conducted on an atomic force microscope (AFM, Bruker, Dimension FastScan) in tapping mode. The experimental temperature was 18 °C.

The photo-welded bilayer films were fabricated using the photofluidization, in which the films (thickness: 20 μm) were exposed to UV light (365 nm, 100 mW cm^{-2}) for 2 min. Then, the fluidized films were overlapped with each other, pressed with a 200 g weight for 5 min, and finally cured by irradiation with visible light (530 nm, 60 mW cm^{-2}) for about 2 min. The cross-sectional SEM images of photo-welded films were investigated using a field-emission scanning electron microscope (FESEM, Zeiss, Ultra 55). All cross-sectional samples were fractured after dipping into liquid nitrogen. The elastic moduli of drop-cast films and photo-welded films were measured with a tensile machine (Instron, Series 5943) at a loading rate of 20 mm min^{-1} at ambient temperature and each test was repeated at least 6 times to allow for statistical analysis. The samples were of the same size (20 mm × 3 mm × 20 μm), and the photo-welded area of all LCP films has the same size (3 mm × 3 mm).

Photoinduced bending behavior of LCP films

The textures of the LCP were observed using a polarizing optical microscope (POM, OPTEC, BK-Pol). 2D X-ray diffraction (2D-XRD) experiments of the LCP films were conducted on a small angle/wide angle diffractometer (Xeuss 2.0) with a 2D detector of Pilatus3R in transmission mode. Grazing incidence X-ray diffraction (GIXRD) experiments of P1 films were conducted on the same instrument in out-of-plane mode. The X-ray sources (Cu Kα, λ = 0.154 nm) were produced by 3 kW ceramic tubes and the peak positions were calibrated with silicon powder ($2\theta > 15^{\circ}$) and silver behenate ($2\theta < 10^{\circ}$). Photographs and videos of the LCP deformation behaviors were taken using a super-resolution digital microscope (Keyence, VHX-1000C).

Results and discussion

Photofluidization of LCP films

The photofluidization of azobenzene-containing LCPs stems from the photoswitching of T_g, which is closely related to the chemical structures of side chain groups.[42,43] The azobenzene monomer was copolymerized with cyclooctene, rigid biphenyl, and flexible phenyl benzoate monomers to synthesize P1, P2, and P3 by ROMP, respectively (Fig. 2a). The molar ratio of the azobenzene monomer to the non-photoresponsive monomer was constant (2 : 1). Thanks to this living polymerization process, the molecular weights of the LCPs ($\sim 2 \times 10^5$ g mol^{-1}, Fig. S4 and Table S1, ESI†) are close to each other and at least one order of magnitude larger than those of the general LCPs.[44]

Upon UV irradiation, the *trans* LCPs isomerized to the *cis* state with a high *trans–cis* photoconversion efficiency (>96%), which was investigated using the UV-Vis spectra (Fig. S5 and S6, ESI†). Therefore, *cis* LCPs were prepared according to the published work.[38] The T_g of the LCPs at *trans* and *cis* states was measured by the DSC measurement. The DSC heating curves show a near-room-temperature T_g of the *trans* LCPs and a subzero T_g of the *cis* LCPs, indicating that the *cis* LCPs are in a rubbery state or a viscous flow state (Fig. 2b). The viscosity measured using the rotational rheometer increases rapidly when the frequency is lower than 1 Hz, indicating that the *cis* P1 is in the rubbery state rather than the viscous flow state (Fig. S7, ESI†). Similarly, both *cis* P2 and *cis* P3 are in the rubbery state. The T_g of *cis* P1 is the lowest, which may result from the low density of side chains. On the other hand, the non-responsive mesogens of *cis* P2 and *cis* P3 restrict the motility of chain segments to some extent. In addition, two small endothermic peaks emerge between the T_g (30 °C) and the clearing temperature (78 °C) in the DSC heating curve of *trans* P1, indicating the transition temperature of the smectic phase accompanied by the degree of decline of the order.

We performed nanoindentation measurements and quantitative nanoscale mechanical characterization by AFM on the drop-cast LCP films (thickness: 20 μm) to study the influence of photofluidization on the mechanical properties of the surface (Fig. 2c). The loading–pause–unloading displacement curves show that upon *trans–cis* isomerization induced by UV light, the hard surface of the LCP films gradually transfers to a soft state, leading to a significantly increased penetration depth and an obvious creep phenomenon (Fig. 2d). This variation is attributed to the fact that the surface is in the rubbery state possessing T_g below room temperature. In addition, the unloading curves reveal that compared to *cis* P2 and *cis* P3 that undergo an elastic–plastic deformation, *cis* P1 exhibits a typical plastic deformation, resulting from the lower density of side chains and a larger free volume. As summarized in Table 1, the hardness of all the LCP films decreases by one order of magnitude after UV irradiation. P1 exhibited the largest change of 96%, indicating the best photofluidization effect.

The retract force-separation curves of all the *trans* LCP films show a tiny action distance (<10 nm) between the tip and the surface with a negligible adhesion force (<50 nN) (Fig. 2e). After UV irradiation, the surface adhesion force of *cis* P1 and *cis* P3 is obviously increased, resulting from the increase of surface polarity based on the photoisomerization of the azobenzene groups (Table 1). In addition, due to the higher intermolecular force which stems from the lower density of side chains, *cis* P1

Table 1 The surface hardness and adhesion of *trans* and *cis* LCP films

LCP films		Surface hardness (MPa)	Surface adhesion (nN)
P1	*trans*	67.7 ± 2.6	14.8 ± 2.3
	cis	2.5 ± 0.3	294.6 ± 4.7
P2	*trans*	57.7 ± 3.3	22.2 ± 3.8
	cis	4.1 ± 0.4	27.0 ± 1.9
P3	*trans*	22.1 ± 1.4	36.8 ± 1.6
	cis	2.7 ± 0.5	181.7 ± 3.6

exhibits a higher adhesion force and a larger action distance than *cis* P3. Compared to *cis* P1 and *cis* P3, the lowest adhesion force of *cis* P2 may stem from the biphenyl mesogens in the side chains. The strong π–π stacking leads to the poor mobility of molecular segments and the symmetric chemical structure causes the low surface polarity, both of which result in the low surface adhesion. In summary, the aforementioned experimental results illustrate that P1 film has the lowest hardness and the largest adhesion force upon UV light irradiation, indicating the best photofluidization effect.

Photo-welding of LCP films

Three photo-welded bilayer films were fabricated through the surface photofluidization process of P1, P2, and P3 films, respectively (please see Experimental for the photo-welding procedure). The cross-sectional SEM images show that both P1 and P3 films are photo-welded seamlessly, which originates from the fusion of two fluidized surfaces by pressure (Fig. 3a and c).

We introduced the rhodamine dye in the LCP films to observe the diffusion in the photo-welded films. The rhodamine-containing LCP films were fabricated by the drop-casting method and photo-welded with the original films under pressure (200 g). The obtained bilayer films were fractured after dipping into liquid nitrogen, and the cross-sectional color was observed using a microscope (Fig. S8, ESI†). The microscopic images show a clear color gradation region at the center of the bilayer P1 and P3 films, which reveals that the UV-irradiated surface of two films diffuses together due to pressure. The experiment proves the existence of the fusion region, which results from the cross-diffusion of the fluidized surface. Taking advantage of the extraordinary photo-fluidization, the surface of P1 films transfers to a fluidized state with high adhesion force upon UV irradiation, which is beneficial to surface physical fusion between two films. The adequate entanglement of chain segments in the fusion area enhances the solidity and stability of photo-welding. However, in contrast to P1 and P3, the bilayer film of P2 has no color gradation region with a clear boundary and several gaps (Fig. 3b), indicating a poor photo-welding result.

It is worth noting that the photo-welding process is athermal, which is testified by the temperature variation of the P1 film recorded with an infrared thermography. The photographs illustrate that the temperature of the film increases by only 6 °C after UV irradiation (365 nm, 100 mW cm^{-2}) for 2 min, and then decreases to room temperature within 1 min after the UV light is turned off (Fig. S9, ESI†). The photo-welded strip exhibits strong robustness bearing a weight of 150 g, which is ascribed to the high molecular weight and the excellent photo-welding effect (Fig. 3d).

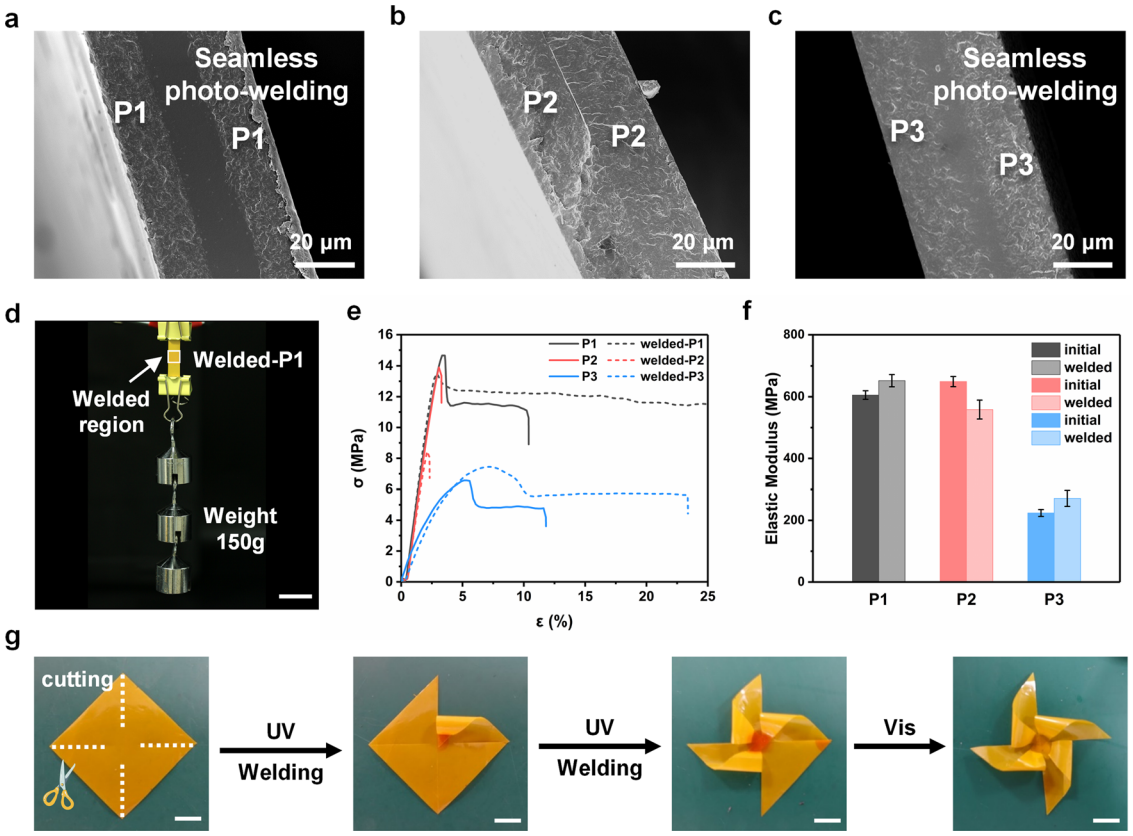

Fig. 3 Photo-welding of LCP films. (a–c) Cross-sectional SEM images of the P1, P2, and P3 films. (d) A photograph showing that the photo-welded P1 film is capable of hanging 150 g weights. The scale bar is 20 mm. (e) Stress–strain curves of the original and the photo-welded films. (f) A plot showing the elastic moduli of the original and the photo-welded films. (g) Photographs showing the process of constructing a photo-welded windmill. UV: 365 nm, 100 mW cm^{-2}, 2 min. Visible light: 530 nm, 60 mW cm^{-2}, 2 min. The scale bar is 10 mm.

To study the stability of the photo-welded films, the mechanical properties of the original drop-cast films and photo-welded films were measured using a tensile method, respectively (Fig. 3e and f). The low breaking elongation of the photo-welded P2 film illustrates the poor photo-welding result with a lower elastic modulus than that of the initial film. The stress–strain curves of photo-welded P1 and P3 films show an increased breaking elongation with a larger yield strain, indicating the great effect of photo-welding. The elastic moduli of photo-welded P1 and P3 films are slightly increased compared to those of the initial films, probably as a result of the twice thickness of the welded area. It should be noted that none of the stretched films fractured at the welded area (Movie S1, ESI†), which proved the stability and excellent mechanical properties of the welded region.

Although P3 films were seamlessly welded, the mechanical properties of P3 were not strong enough to build a free-standing functional actuator. Therefore, P1 is chosen as the optimum material for building photodeformation 3D actuators. An LCP windmill was produced *via* a photo-welding process in combination with the tailoring method, in which the welding region was precisely controlled by the light (Fig. 3g). The linear structure of the LCPs and none of the auxiliary adhesives allow for directly recycling the materials by solvent dissolution or melting.

Photoinduced bending behaviors of the stretched P1 films

The excellent deformation performance of LCPs requires an appropriate orientation method to obtain an ordered alignment of mesogens. The thermal stretching method is chosen because it is easy to operate for obtaining a uniaxial orientation. The 40 μm-thick drop-cast films were stretched to a certain length in a 60 °C oven and fixed for about 20 min to release the stress. LCP films with diverse stretching ratios ($(l - l_0)/l_0 \times 100\%$, l denotes the length of the stretched film, l_0 denotes the length of the initial film) of 100%, 200%, 300%, and 400% were prepared by this method, respectively. The thickness of the stretched films is 25 μm, 20 μm, 15 μm, and 10 μm with stretching ratios of 100%, 200%, 300%, and 400%, respectively. In order to compare the orientation degree of the films obtained at different stretching ratios, we characterized the LC orientation of the films by the POM and 2D-WAXD, where the X-ray beam was applied from the side of the films (Fig. S10, ESI†). The ring-shaped diffraction pattern of the original film suggests the chaotic and polydomain mesogens. With the increase of the stretching ratio, diffractive arcs in the wide-angle region gradually gather at the equatorial location, indicating that the mesogens are oriented along the stretching direction. The diffractive arcs in the small-angle region split into mutually symmetrical diffraction spots, demonstrating the formation of a highly ordered smectic C phase. When the stretching ratio of the P1 film is larger than 200%, an obvious bright-dark change is observed by rotating the POM stage, which proves the formation of a monodomain orientation of mesogens.

The photoinduced bending behaviors of the stretched films were recorded by a super-resolution digital microscope, and at least five samples were experimented to ensure the reliability of the results (Fig. S11, Fig. 4a and Movie S2, ESI†). All the films

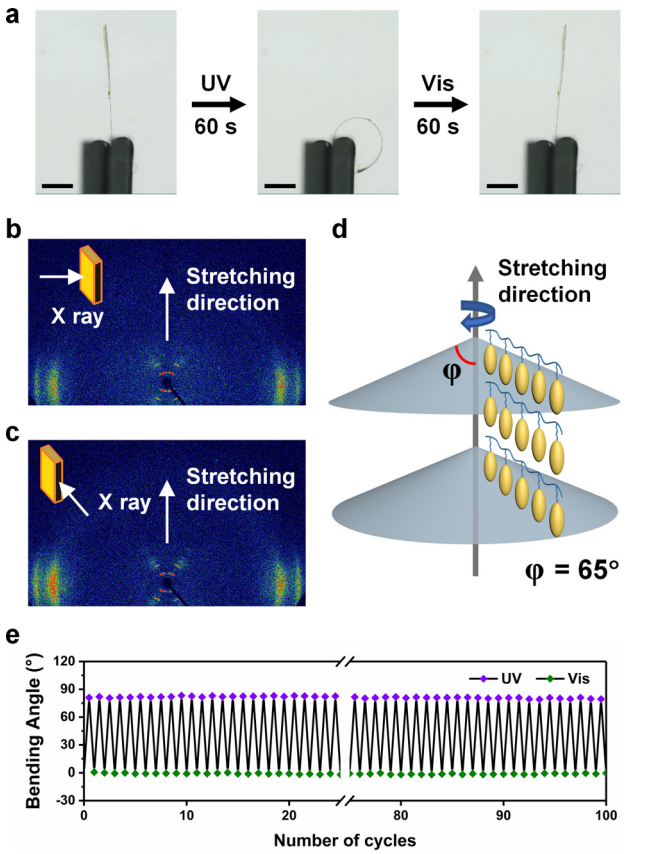

Fig. 4 (a) Photographs showing the photo-induced bending behavior of the stretched P1 film (300%) by alternative irradiation with UV (365 nm, 30 mW cm^{-2}) and visible light (530 nm, 30 mW cm^{-2}). The films were cut into long strips (8 mm × 4 mm) along the stretching direction. The scale bar is 2 mm. (b and c) The 2D-WAXD patterns of stretched P1 film and the X-ray beam is applied to the front and the side of the film. (d) Schematic illustration of the mesogen orientation in the stretched film. (e) A plot showing the reversible bending of the stretched P1 film on alternative irradiation with UV (365 nm, 30 mW cm^{-2}) and visible light (530 nm, 30 mW cm^{-2}) for 100 cycles.

exhibit bending behaviors away from the light upon UV illumination (365 nm, 30 mW cm^{-2}) and return to the initial state upon exposure to visible light (530 nm, 30 mW cm^{-2}). The bending angle of the films with the stretching of 300% is significantly larger than that of the films at 200%, while the bending angles of the films at 300% and 400% are similar, indicating that the mesogens are oriented completely when the film is stretched to a ratio of 300%. Hence, the following experiments were conducted using the films with a stretching ratio of 300%.

It is worth noting that azobenzene-containing LCP films with a planar uniaxial orientation generally exhibit bending toward the irradiation direction of the light since an anisotropic contraction is generated along the orientation direction upon UV irradiation.[20] Interestingly, our stretched P1 films bent away from the UV light. To investigate the photodeformation mechanism, we performed 2D-WAXD characterization with the X-ray beam applied to the front and the side of the film (Fig. 4b and c). The diffraction spots of the two patterns are almost the same,

and the azimuthal integration indicates that the tilting angle (φ) of the mesogens in the smectic C phase is 65° (Fig. S12, ESI†). Therefore, it can be inferred that the LC layers are distributed as a stacked umbrella-like structure, and the mesogens are all oriented along the stretching direction (Fig. 4d). The GIXRD diffraction patterns show that the LC layer structure in the surface of the film is nearly identical after UV (365 nm, 30 mW cm^{-2}, 60 s) and visible light (530 nm, 30 mW cm^{-2}, 60 s) illumination (Fig. S13, ESI†). Considering the special layer structure of LC alignment, we assume that such a photoinduced bending behavior originates from the anisotropic free volume expansion in the orientation direction of the illuminated surface, where the highly ordered smectic C phase with a densely packed structure requires more free volume for the photoisomerization of azobenzene groups.[45] To verify the free volume expansion of the stretched P1 film under UV illumination, we measured the density of a free-standing film in the UV-illuminated and visible light-illuminated state (Fig. S14, ESI†). First, the stretched P1 film was immersed in the salt solution, whose density (1.0733 g cm^{-3}) was a little bit lower than that of the film, and the film was sinking in the solution. Then the stretched P1 film behaved bending and floated in the solution upon UV illumination, which is ascribed to a decrease in the density of the film, indicating the free volume expansion caused by the photoisomerization of the azobenzene groups (Movie S3, ESI†). When exposed to visible light, the bending film returned to the initial plate state and sank to the bottom of the cuvette, as the density increased to the original state. Moreover, this density variation along with the shape change was reversible.

The P1 films stretched at a ratio of 300% exhibited photodeformation behaviors with a rapid response and excellent reversibility under alternative irradiation with UV (365 nm, 30 mW cm^{-2}, 10 s) and visible light (530 nm, 30 mW cm^{-2}, 10 s), which is ascribed to the physical cross-linking provided by the crystallization of the poly-cyclooctene chain segment (Fig. 4e and Fig. S15, ESI†). Importantly, both the photodeformation and photofluidization depend on the photoisomerization of the azobenzene groups, which can be separately controlled by manipulating the UV light intensity. When UV irradiation with high intensity (> 70 mW cm^{-2}) is applied, the P1 films become soft due to the photofluidization, because more azobenzene groups undergo photoisomerization. The photodeformation behaviors of the films are achieved with low light intensity to avoid softening, since the elastic modulus of the P1 films is nearly constant when the light intensity is lower than 50 mW cm^{-2} (Fig. S16, ESI†).

Photo-welded 3D actuators of P1

We demonstrated various deformations of winding, unwinding, and curling by the P1 films that were cut in different θ, where θ denotes the angle between the stretching direction and the cutting direction (Fig. 5a). All these films have a flat initial

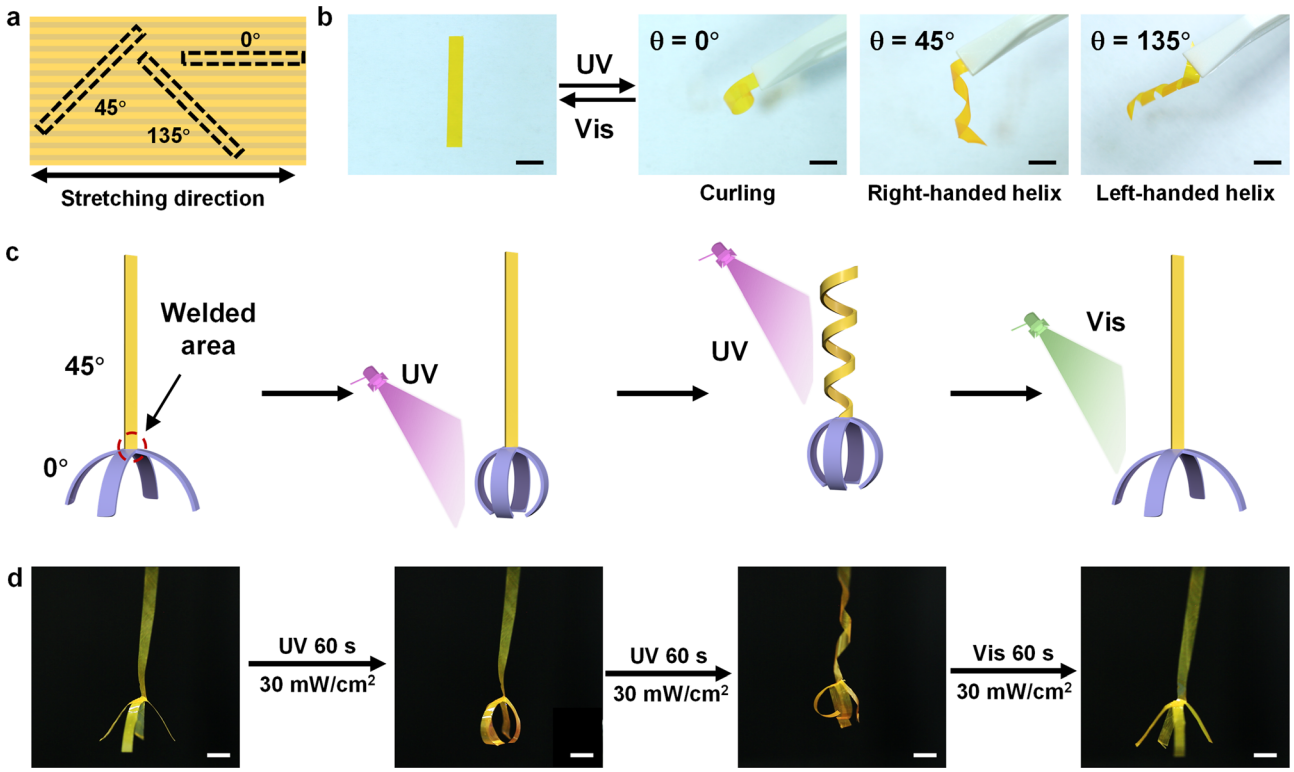

Fig. 5 (a) Schematic illustration of the cutting direction of different ribbons. (b) Photographs showing diverse photodeformation behaviors of the ribbons cut in different directions. θ denotes the angle between the cutting direction and the stretching direction. (c) Schematic diagram of a lifting gripper photo-welded by ribbons cut in different directions. The purple part is built by two ribbons of θ = 0° *via* the photo-welding process, which bends upon UV irradiation (365 nm, 30 mW cm^{-2}) and plays the role of grasping objects. The yellow part serves as a rise and fall controller with a ribbon of θ = 45°, which is capable of winding and unwinding upon alternative UV (365 nm, 30 mW cm^{-2}) and visible irradiation (530 nm, 30 mW cm^{-2}). (d) Photographs showing the photodeformation behaviours of the lifting gripper. The scale bar is 5 mm.

shape but exhibit extremely different photodeformation behaviors upon UV illumination (365 nm, 30 mW cm^{-2}), which are determined by θ (Fig. 5b). The ribbons exhibit curling when θ is 0° and winding when θ are 45° and 135°, which results from the anisotropic expansion of ribbons in the direction of mesogen orientation. The ribbons of $\theta = 45°$ and $\theta = 135°$ revealed a similar winding behavior with opposite handedness because the orientations of mesogens in the two ribbons were mirror symmetric. All the ribbons returned to their original flat state when irradiated with visible light (530 nm, 30 mW cm^{-2}). A cucumber-like vine structure was built by assembling the ribbons of $\theta = 45°$ and $\theta = 135°$ at the end, which exhibited helical deformation behaviors with opposite handedness under UV light (Fig. 1c and Movie S3, ESI†).

A gripper actuator was integrated by the stretched films with diverse deformation modes through the precise photo-welding process. Two ribbons of $\theta = 0°$ were photo-welded in the center and built into a "hand" (purple part in the schematic). A ribbon of $\theta = 45°$ acted as an "arm" (yellow part in the schematic) and was photo-welded with the "hand" to fabricate a lifting gripper (Fig. 5c, d and Movie S4, ESI†). The "hand" of the gripper grabbed and released the objects when the ribbons exhibited curling and straight states with the irradiation of UV and visible light. The "arm" of the gripper acted as a rise and fall controller by changing the degree of spiral deformation upon the irradiation of UV light and visible light. It is worth noting that all the above deformations can be performed quickly and reversibly with good repeatability. It is predictable that the photo-welding process based on photofluidization could have an excellent prospect for applications in the field of assembly of different materials with various deformation modes.

Conclusions

In conclusion, the photofluidization was employed to construct 3D flexible actuators by photo-welding of the azobenzene-containing linear LCPs. Uniaxially oriented LCP films were obtained by the thermal stretching method, exhibiting excellent and reversible photodeformation behaviors. Several deformation modes, such curling, winding, and unwinding, were determined by the different cutting directions of the LCP ribbons, which were subsequently seamlessly photo-welded to integrate 3D actuators based on the photofluidization. Moreover, the influences of the mesogen structures on T_g, surface hardness, and adhesion force of the LCP films were comprehensively investigated to realize the best photofluidization effect. Due to the benefits of light, such as remote access without contact, fixed-point manipulation, and high spatiotemporal resolution, this light-controlled athermal photo-welding technique could provide precise and seamless welding without using additional reagents. Notably, this approach can be applied to any polymers that exhibit the photofluidization, and it also allows for the integration of different materials without structural defects in the welded region.

Author contributions

J. W. and Y. Y. designed the LCPs. Y. F. synthesized and characterized the LCPs. Y. F., L. Q. and Y. Y. designed the photo-welding process and 3D actuators. Y. F. performed the related experiments and characterization of photo-welding. Y. F., L. Q. and Y. Y. discussed the results and analysed the data. Y. F. drafted the manuscript. J. W., L. Q. and Y. Y. revised the manuscript. Y. Y. supervised the research.

Conflicts of interest

There are no conflicts to declare.

Acknowledgements

This work was financially supported by the National Natural Science Foundation of China (21734003, 51721002) and the Natural Science Foundation of Shanghai (20ZR1406700).

References

1 M. Zou, S. Li, X. Hu, X. Leng, R. Wang, X. Zhou and Z. Liu, *Adv. Funct. Mater.*, 2021, **31**, 2007437.
2 M. Wehner, R. L. Truby, D. J. Fitzgerald, B. Mosadegh, G. M. Whitesides, J. A. Lewis and R. J. Wood, *Nature*, 2016, **536**, 451–455.
3 G. Li, X. Chen, F. Zhou, Y. Liang, Y. Xiao, X. Cao, Z. Zhang, M. Zhang, B. Wu, S. Yin, Y. Xu, H. Fan, Z. Chen, W. Song, W. Yang, B. Pan, J. Hou, W. Zou, S. He, X. Yang, G. Mao, Z. Jia, H. Zhou, T. Li, S. Qu, Z. Xu, Z. Huang, Y. Luo, T. Xie, J. Gu, S. Zhu and W. Yang, *Nature*, 2021, **591**, 66–71.
4 P. Won, K. Kim, H. Kim, J. Park, I. Ha, J. Shin, J. Jung, H. Cho, J. Kwon, H. Lee and S. Ko, *Adv. Mater.*, 2021, **33**, e2002397.
5 H. Zhou, C. C. Mayorga-Martinez, S. Pane, L. Zhang and M. Pumera, *Chem. Rev.*, 2021, **121**, 4999–5041.
6 J. Lv, Y. Liu, J. Wei, E. Chen, L. Qin and Y. Yu, *Nature*, 2016, **537**, 179–184.
7 T. Ikeda and O. Tsutsumi, *Science*, 1995, **268**, 1873–1875.
8 S. Han, Y. Chen, B. Xu, J. Wei and Y. Yu, *Chin. J. Polym. Sci.*, 2020, **38**, 806–813.
9 F. Cheng, R. Yin, Y. Zhang, C. Yen and Y. Yu, *Soft Matter*, 2010, **6**, 3447–3449.
10 M. Rogóż, H. Zeng, C. Xuan, D. Wiersma and P. Wasylczyk, *Adv. Opt. Mater.*, 2016, **4**, 1689–1694.
11 Z. Nie, B. Zuo, M. Wang, S. Huang, X. Chen, Z. Liu and H. Yang, *Nat. Commun.*, 2021, **12**, 2334.
12 F. Zhai, Y. Feng, Z. Li, Y. Xie, J. Ge, H. Wang, W. Qiu and W. Feng, *Matter*, 2021, **4**, 3313–3326.
13 M. Pilz da Cunha, S. Ambergen, M. G. Debije, E. F. G. A. Homburg, J. M. J. den Toonder and A. P. H. J. Schenning, *Adv. Sci.*, 2020, **7**, 1902842.
14 X. Lu, S. Guo, X. Tong, H. Xia and Y. Zhao, *Adv. Mater.*, 2017, **29**, 1606467.
15 A. Kotikian, C. McMahan, E. C. Davidson, J. M. Muhammad, R. D. Weeks, C. Daraio and J. A. Lewis, *Sci. Rob.*, 2019, **4**, eaax7044.
16 Y. Xiao, Z. Jiang, X. Tong and Y. Zhao, *Adv. Mater.*, 2019, **31**, 1903452.

17 Y. Cheng, H. Lu, X. Lee, H. Zeng and A. Priimagi, *Adv. Mater.*, 2020, **32**, 1906233.
18 X. Pang, J. Lv, C. Zhu, L. Qin and Y. Yu, *Adv. Mater.*, 2019, **31**, e1904224.
19 L. Qin, X. Liu and Y. Yu, *Adv. Opt. Mater.*, 2021, **9**, 2001743.
20 M. Kondo, Y. Yu and T. Ikeda, *Angew. Chem., Int. Ed.*, 2006, **45**, 1378–1382.
21 L. T. de Haan, C. Sanchez-Somolinos, C. M. W. Bastiaansen, A. P. H. J. Schenning and D. J. Broer, *Angew. Chem., Int. Ed.*, 2012, **51**, 12469–12472.
22 L. T. de Haan, V. Gimenez-Pinto, A. Konya, T.-S. Nguyen, J. M. N. Verjans, C. Sánchez-Somolinos, J. V. Selinger, R. L. B. Selinger, D. J. Broer and A. P. H. J. Schenning, *Adv. Funct. Mater.*, 2014, **24**, 1251–1258.
23 S.-k. Ahn, T. H. Ware, K. Lee, V. P. Tondiglia and T. J. White, *Adv. Funct. Mater.*, 2016, **26**, 5819–5826.
24 H. Aharoni, Y. Xia, X. Zhang, R. D. Kamien and S. Yang, *Proc. Natl. Acad. Sci. U. S. A.*, 2018, **115**, 7206–7211.
25 Z. Pei, Y. Yang, Q. Chen, E. M. Terentjev, Y. Wei and Y. Ji, *Nat. Mater.*, 2014, **13**, 36–41.
26 M. Liu, S. Zhu, Y. Huang, Z. Lin, W. Liu, L. Yang and D. Ge, *Composites, Part B*, 2021, **214**, 108748.
27 X. Chen, R. Wang, C. Cui, L. An, Q. Zhang, Y. Cheng and Y. Zhang, *Chem. Eng. J.*, 2022, **428**, 131212.
28 X. Zheng, S. Guan, C. Zhang, T. Qu, W. Wen, Y. Zhao and A. Chen, *Small*, 2019, **15**, e1900110.
29 Y. Zhang, Z. Wang, Y. Yang, Q. Chen, X. Qian, Y. Wu, H. Liang, Y. Xu, Y. Wei and Y. Ji, *Sci. Adv.*, 2020, **6**, eaay8606.
30 Z. Pei, Y. Yang, Q. Chen, Y. Wei and Y. Ji, *Adv. Mater.*, 2016, **28**, 156–160.
31 L. Chen, M. Wang, L. Guo, B. Lin and H. Yang, *J. Mater. Chem. C*, 2018, **6**, 8251–8257.
32 M. O. Saed, A. Gablier and E. M. Terentejv, *Adv. Funct. Mater.*, 2019, **30**, 1906458.
33 L. Chen, H. Bisoyi, Y. Huang, S. Huang, M. Wang, H. Yang and Q. Li, *Angew. Chem., Int. Ed.*, 2021, **60**, 16394–16398.
34 M. Tan, G. Thangavel and P. Lee, *Adv. Funct. Mater.*, 2021, **31**, 2103097.
35 W. Xu, S. Sun and S. Wu, *Angew. Chem., Int. Ed.*, 2019, **58**, 9712–9740.
36 M. Chen, S. Liang, C. Liu, Y. Liu and S. Wu, *Front. Chem.*, 2020, **8**, 706.
37 S. Liang, C. Nie, J. Yan, Q. Zhang and S. Wu, *Chin. J. Polym. Sci.*, 2020, **39**, 1225–1234.
38 H. Zhou, C. Xue, P. Weis, Y. Suzuki, S. Huang, K. Koynov, G. K. Auernhammer, R. Berger, H.-J. Butt and S. Wu, *Nat. Chem.*, 2017, **9**, 145–151.
39 M. Chen, B. Yao, M. Kappl, S. Liu, J. Yuan, R. Berger, F. Zhang, H.-J. Butt, Y. Liu and S. Wu, *Adv. Funct. Mater.*, 2020, **30**, 1906752.
40 B. Xu, C. Zhu, L. Qin, J. Wei and Y. Yu, *Small*, 2019, **15**, e1901847.
41 X. Pang, L. Qin, B. Xu, Q. Liu and Y. Yu, *Adv. Funct. Mater.*, 2020, **30**, 2002451.
42 H. Akiyama, T. Fukata, A. Yamashita, M. Yoshida and H. Kihara, *J. Adhes.*, 2016, **93**, 823–830.
43 P. Weis, A. Hess, G. Kircher, S. Huang, G. K. Auernhammer, K. Koynov, H.-J. Butt and S. Wu, *Chemistry*, 2019, **25**, 10946–10953.
44 X. Li, L. Fang, L. Hou, L. Zhu, Y. Zhang, B. Zhang and H. Zhang, *Soft Matter*, 2012, **8**, 5532–5542.
45 Z. Cheng, S. Ma, Y. Zhang, S. Huang, Y. Chen and H. Yu, *Macromolecules*, 2017, **50**, 8317–8324.